

LEARNED IMAGE DOWNSCALING FOR UPSCALING USING CONTENT ADAPTIVE RESAMPLER

Wanjie Sun and Zhenzhong Chen*

School of Remote Sensing and Information Engineering, Wuhan University

ABSTRACT

Deep convolutional neural network based image super-resolution (SR) models have shown superior performance in recovering the underlying high resolution (HR) images from low resolution (LR) images obtained from the predefined downscaling methods. In this paper we propose a learned image downscaling method based on content adaptive resampler (CAR) with consideration on the upscaling process. The proposed resampler network generates content adaptive image resampling kernels that are applied to the original HR input to generate pixels on the downscaled image. Moreover, a differentiable upscaling (SR) module is employed to upscale the LR result into its underlying HR counterpart. By back-propagating the reconstruction error down to the original HR input across the entire framework to adjust model parameters, the proposed framework achieves a new state-of-the-art SR performance through upscaling guided image resamplers which adaptively preserve detailed information that is essential to the upscaling. Experimental results indicate that the quality of the generated LR image is comparable to that of the traditional interpolation based method, but the significant SR performance gain is achieved by deep SR models trained jointly with the CAR model. The code is publicly available on: URL <https://github.com/sunwj/CAR>.

1 INTRODUCTION

As the smartphone cameras are starting to rival or beat DSLR cameras, a large number of ultra high resolution images are produced everyday. However, it is always reduced from its original resolution to smaller sizes that are fit to the screen of different mobile devices and web applications. Thus, it is desirable to develop efficient image downscaling and upscaling method to make such application more practical and resources saving by only generating, storing and transmitting a single downscaled version for preview and upscaling it to high resolution when details are going to be viewed. Besides, the pre-downscaling and post-upscaling operation also helps to save storage and bandwidth for image or video compression and communication [1, 2, 3, 4].

Image downscaling is one of the most common image processing operations, aiming to reduce the resolution of the high-resolution (HR) image while keeping its visual appearance. But according to the Nyquist-Shannon sampling theorem [5], it is inevitable that high-frequency content will get lost during the sample-rate conversion. Contrary to the image downscaling task is the image upscaling, also known as resolution enhancement or super-resolution (SR), trying to recover the underlying HR image of the LR input. Image SR is essentially an ill-posed problem because an undersampled image could refer to numerous HR images. The quality of the SR result is very limited due to the ill-posed nature of the problem and the lost frequency components cannot be well-recovered [6, 7]. Previous work regards image downscaling and SR as independent tasks. Image downscaling techniques pay much attention to enhance details, such as edges, which helps to improve human visual perception [3]. On the other hand, recent state-of-the-art deep SR models have witnessed their capability to restore HR images from the

LR version downscaled using traditional filtering-decimation based methods with great performance gain [8, 9]. However, the predetermined downscaling operations may be sub-optimal to the SR task and state-of-the-art deep SR models still cannot well recover detailed information from distorted textures caused by the fixed downscaling operations.

In this paper, we proposed a learned content adaptive image downscaling model in which an SR model tries to best recover the HR images while adaptively adjusting the downscaling model to produce LR images with potential detailed information that are key to the optimal SR performance. The downscaling model is trained without any LR image supervision, and to make sure that the LR image produced by our downscaling model is a valid image, we propose to employ the resampling method where content adaptive non-uniform resampling kernels predicted by a convolutional neural network (CNN) are applied to the original HR image to generate pixels of the LR output. Quantitative and qualitative experimental results illustrate that LR images produced by the proposed model can maintain comparable visual quality as the widely used bicubic interpolation method while advanced SR image quality is obtained using state-of-the-art deep SR models.

Our contributions are concluded as follows:

- A learned image downscaling model is proposed which is trained under the guidance of the SR model. The proposed image downscaling model produces images that can be well super-resolved and are capable of maintaining comparable visual quality. Experimental results indicate a new state-of-the-art SR performance with the proposed end-to-end image downscaling and upscaling framework.
- The resampling method is employed to downscale image by applying content adaptive non-uniform resampling kernels on the original HR input for each pixel on the LR output, which can effectively maintain the

This work was supported in part by National Natural Science Foundation of China under contract No. 61771348. (Corresponding author: Zhenzhong Chen, E-mail: zzchen@ieee.org)

structure of the HR input in an unsupervised manner. Because directly predicting the LR image by combining low and high-level abstract image features can not guarantee that the generated result is a genuine image without any LR image supervision.

- The learned content adaptive non-uniform resampling kernels perform non-uniform sampling and also make the size of resampling kernels to be more effective. The learned content adaptive non-uniform resampling kernels are composed of weights and sampling position offsets in both horizontal and vertical directions, making the learned resampling kernels adaptively change their weights and shape according to their corresponding resampling contents.

The rest of the paper is organized as follows. Section 2 reviews task independent and task driven image downscaling algorithms. Section 3 introduces the proposed SR guided content adaptive image downscaling framework, and computing process of each component in the framework is explained. Section 4 evaluates and analyzes experimental results for the SR images and down-scaled images quantitatively and qualitatively. Finally, Section 5 summarizes our work.

2 RELATED WORK

This section presents a review about image downscaling techniques aiming to maintain the visual quality of the LR image. Image downscaling algorithms can be categorized into two groups as follows.

2.1 Task independent image downscaling

Earlier work of image downscaling primarily tends to prevent aliasing [5] which arises during sampling rate reduction. Those methods are based on linear filters [10], where the HR image is firstly convolved with the low-pass kernel to push the image below the Nyquist frequency [11], then being sub-sampled into target size. Many frequency-based filters are developed, *e.g.*, the box, bilinear and bicubic filter [12]. However, the down-scaled images tend to be blurred because the high-frequency details are suppressed. Filters that are designed to model the ideal *sinc* filter, *e.g.*, the Lanczos filter [13], tend to produce ringing artifacts near strong image edges. All of these filters are predetermined with some of them having tuning parameters. The same filter is applied globally to the input HR image, ignoring characteristics of image content with varying details.

Recently, many researchers begin to focus on the aspects of detail preserving and human perception when developing image downscaling algorithm. Kopf *et al.* firstly proposed a novel content adaptive image downscaling method based on a joint bilateral filter [14]. The key idea is to optimize the shape and locations of the downsampling kernels to better align with local image features by considering both spatial and color variances of the local region. Öztireli and Gross [15] proposed a method to downscale HR images without filtering. They consider image downscaling as an optimization problem and use the structural similarity index (SSIM) [16] as objective to directly optimize the down-scaled image against its original image, and this approach helps to capture most of the perceptually important details. Weber *et al.* [17] proposed an image downscaling algorithm aiming

to preserve small details of the input image, which are often crucial for a faithful visual impression. The intuition is that small details transport more information than bigger areas with similar colors. To that end, an inverse bilateral filter is used to emphasize differences rather than punishing them. Gastal and Oliveira [18] introduced the spectral remapping algorithm to control aliasing during image downscaling. Instead of discarding high-frequency information, it remaps such information into the representable range of downsampled spectrum. Recently, Liu *et al.* [19] proposed a L0-regularized optimization framework for image downscaling, which is composed of a gradient-ratio prior and reconstruction prior. The downscaling problem is solved by iteratively optimize the two priors in an alternative way.

2.2 Task specific image downscaling

Most image downscaling algorithms only care about the visual quality of the down-scaled image, so that the down-scaled image may not be optimal to other computer vision tasks. To tackle this problem, task guided image downscaling has emerged. Zhang *et al.* [3] took the quality of the interpolated image from the down-scaled counterpart into consideration. They proposed an interpolation-dependent image downscaling algorithm by modeling the downscaling operation as the inverse operator of up-sampling. Benefiting from the well established deep learning frameworks, Hou *et al.* [20] proposed a deep feature consistency network that is applicable to image mapping problems. One of the applications illustrated in the paper is image downscaling. The image downscaling network is trained by keeping the deep features of the input HR image and resulting LR image consistent through another pre-trained deep CNN. Kim *et al.* [21] presented a task aware image downscaling model based on the auto-encoder and the bottleneck layer outputs the down-scaled image. In their framework, the encoder acts as the image downscaling network and the decoder is the SR network. The task aware down-scaled image is obtained by jointly training the encoder and decoder to maximize the SR performance. Similar to the framework presented by [21], Li *et al.* [4] proposed a convolutional neural network for image compact resolution named CNN-CR, which is composed of a CNN to estimate the LR image and a learned or specified upscaling model to reconstruct the HR image. Although the above three mentioned methods did not employ any ground-truth LR image, the generative nature of the encoder like networks implicitly require additional information to constrain the output to be a valid image whose content resembles the HR image. In [20], in order to compute feature consistency loss against the HR image, they upsample the down-scaled image back to the same size as the HR input using nearest neighbor interpolation. In [21, 4], guidance images, obtained using bicubic down-sampling, are employed to constrain the output space of the LR image generating networks.

3 MODEL ARCHITECTURE

This section introduces the architecture and formulation of the content adaptive resampler (CAR) model for image downscaling. As shown in Fig. 1, the framework is composed of two major components, *i.e.*, the resampler generation network (ResamplerNet) and the SR network (SRNet). The ResamplerNet is responsible for estimating the content adaptive resampling kernels according to its input HR image, later the resampling

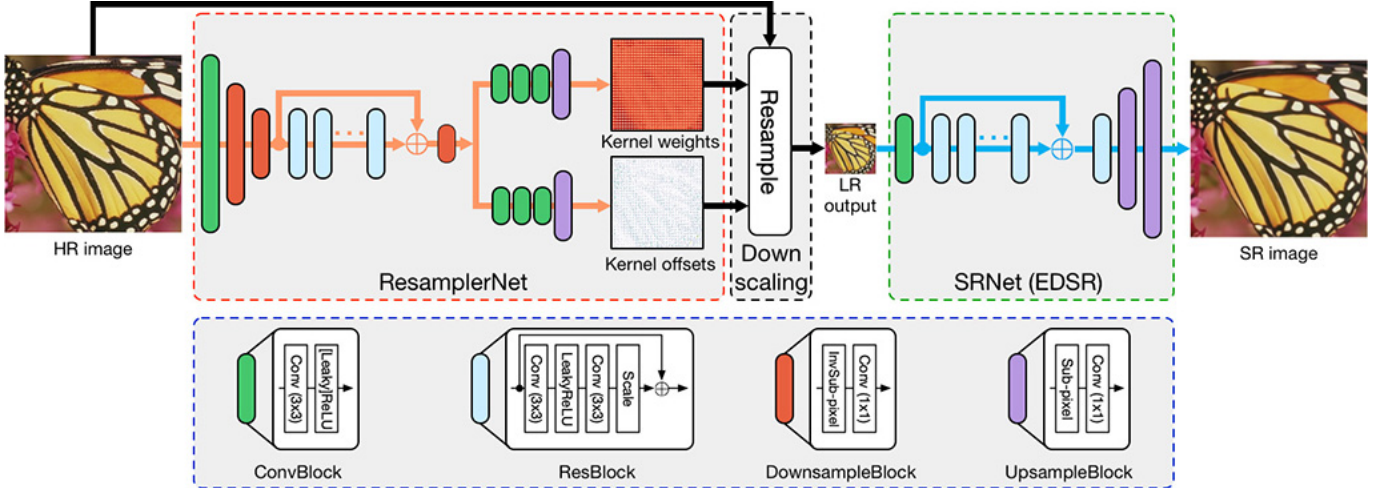


Figure 1: Network architecture. It consists of three parts, the ResamplerNet, the Downscaling module, and the SRNet. The ResamplerNet is designed to estimate content adaptive resampling kernels and its corresponding offsets for each pixel in the downsampled image. The SRNet, on the other hand, takes the resulting downsampled image as input and tries to restore the underlying HR image. The entire framework is trained end-to-end in an unsupervised manner where the primary objective we need to optimize is the SR reconstruction error with respect to the input HR image. By back-propagating the reconstruction error through the SRNet and ResamplerNet, it adjusts the resampler generation network to produce better resampling kernels which make the downsampled image can be super-resolved more easily.

kernels are applied to the input HR image to produce the downsampled image. The SRNet, on the other hand, takes the resulting downsampled image as input and tries to restore the underlying HR image. The entire framework is trained end-to-end in an unsupervised manner where the primary objective we need to optimize is the SR reconstruction error with respect to the input HR image. By back-propagating the reconstruction error through the SRNet and ResamplerNet, it adjusts the resampler generation network to produce better resampling kernels which make the downsampled image can be super-resolved more easily.

3.1 Content adaptive image downscaling resampler

We design the proposed content adaptive image downscaling model that is trained using the unsupervised strategy. Unlike work presented in [20, 21, 4] which synthesizes the downsampled image by combining latent representations of the HR image extracted by the CNN, and proper constraints are required to make sure that the result is a meaningful image. We propose to obtain the downsampled image using the idea of resampling the HR image, which effectively makes the downsampled result look like the original HR image without any constraints.

The filters for traditional bilinear or bicubic downscaling are basically fixed, with the only variation being the shift of the kernel according to the location of the newly created pixel in the downsampled image. Contrary to this, we propose to use dynamic downscaling filters inspired by the dynamic filter networks [22]. The downscaling kernels are generated for each pixel in the downsampled image depending on the effective resampling region on the HR image. It can be considered as one type of meta-learning [23] that learns how to resample. However, filter-based image resampling methods generally require a certain minimum kernel size to be effective [19]. We alleviate this issue by taking the idea from the deformable convolutional networks [24]. In addition to estimating the content adaptive resampling kernel

weights, we also associate spatial offsets with each element in the resampling kernel. The content adaptive resampling kernels with position offsets can be considered as learnable dilated (atrous) convolutions [25] with the learned dilated rate. Besides, the offset for each kernel element can be different in both magnitude and direction, it can perform non-uniform sampling according to the content structure of the input HR image.

We use a convolutional neural network with residual connections [26] to estimate the weights and offsets for each resampling kernel. The ResamplerNet consists of downscaling blocks, residual blocks and upscaling blocks. The downscaling and residual blocks are trained to model the context of the input HR image as a set of feature maps. Then, two upscaling blocks are used to learn the content adaptive resampling kernel weights $\mathbf{K} \in \mathbb{R}^{(h/s) \times (w/s) \times m \times n}$, offsets in the horizontal direction $\Delta \mathbf{Y} \in \mathbb{R}^{(h/s) \times (w/s) \times m \times n}$ and offsets in the vertical direction $\Delta \mathbf{X} \in \mathbb{R}^{(h/s) \times (w/s) \times m \times n}$, respectively. h and w are the height and width of the input HR image, s is the downscaling factor, and m, n represent the size of the content adaptive resampling kernel. Each kernel is normalized so that elements of a kernel are summed to be 1.

3.2 Image downscaling

After the content adaptive resampling kernels are estimated, they are applied to the corresponding positions of the input HR image to construct the pixel in the downsampled image. For each output pixel, the same resampling kernel is simultaneously applied to three channels of the RGB image, and as illustrated by Fig. 2 the pixels covered by the resampling kernel are weights summed to obtain the pixel value in the downsampled image.

Forward pass. Firstly, we need to position each resampling kernel, associated with the pixel of the downsampled image, on the HR image. It can be achieved using the projection operation

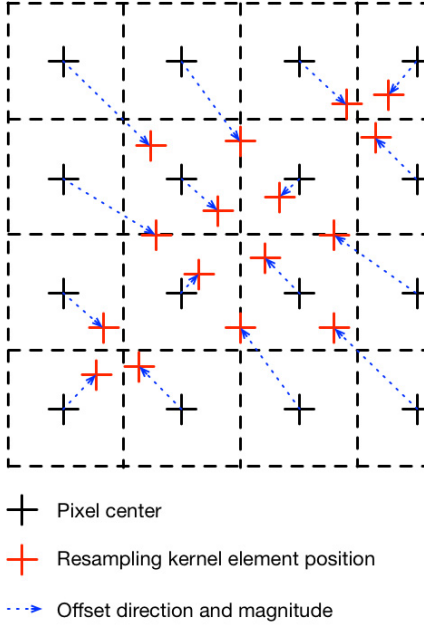


Figure 2: Non-uniform resampling. The black + represents the center of a pixel in the HR image and the red + indicate the position of the resampling kernel element. The blue dashed arrow shows the offset direction and magnitude of the resampling kernel element relative to its corresponding pixel center.

defined as:

$$(u, v) = (x + 0.5, y + 0.5) \times scale - 0.5 \quad (1)$$

where (x, y) is the indices of the pixel at the x -th row and y -th column in the downsampled image, $scale$ represents the downscaling factor, and the resulting (u, v) is the center of downsampled pixel $\mathbf{p}_{x,y}^{\text{LR}}$ projected on the input HR image. Equation 1 assumes that pixels have a nonzero size, and the distance between two neighboring samples is one pixel.

Then, each pixel in the downsampled image is created by local filtering on pixels in the input HR image with the corresponding content adaptive resampling kernel as follows:

$$\mathbf{p}_{x,y}^{\text{LR}} = \sum_{i=0}^{m-1} \sum_{j=0}^{n-1} \mathbf{K}_{x,y}(i, j) \cdot s_{u', v'}^{\text{HR}} \left(u + i - \frac{m}{2} + \Delta \mathbf{X}_{x,y}(i, j), v + j - \frac{n}{2} + \Delta \mathbf{Y}_{x,y}(i, j) \right) \quad (2)$$

where $\mathbf{K}_{x,y} \in \mathbb{R}^{m \times n}$ is the resampling kernel associated with the downsampled pixel at location (x, y) , $\Delta \mathbf{X}_{x,y} \in \mathbb{R}^{m \times n}$ and $\Delta \mathbf{Y}_{x,y} \in \mathbb{R}^{m \times n}$ are the position offsets for each element in the $\mathbf{K}_{x,y}$. The s^{HR} is the sampling value of the input HR image. Due to the location projection and fractional offsets, s^{HR} can refer to non-lattice point on the HR image, therefore, s^{HR} is computed by bilinear interpolating the nearby four pixels around the fractional position:

$$s_{u', v'}^{\text{HR}} = (1 - \alpha)(1 - \beta) \cdot \mathbf{p}_{\lfloor u' \rfloor, \lfloor v' \rfloor}^{\text{HR}} + \alpha(1 - \beta) \cdot \mathbf{p}_{\lfloor u' \rfloor, \lfloor v' \rfloor + 1}^{\text{HR}} + (1 - \alpha)\beta \cdot \mathbf{p}_{\lfloor u' \rfloor + 1, \lfloor v' \rfloor}^{\text{HR}} + \alpha\beta \cdot \mathbf{p}_{\lfloor u' \rfloor + 1, \lfloor v' \rfloor + 1}^{\text{HR}} \quad (3)$$

where u' and v' are fractional position on the HR image, $\alpha = u' - \lfloor u' \rfloor$ and $\beta = v' - \lfloor v' \rfloor$ are the bilinear interpolation weights.

Backward pass. The ResamplerNet is trained using the gradient descent technique and we need to back-propagate gradients from the SRNet through the resampling operation. The partial derivative of the resampling kernel weight can be formulated as:

$$\frac{\partial \mathbf{p}_{x,y}^{\text{LR}}}{\partial \mathbf{K}_{x,y}(i, j)} = \sum_{c=RGB} s_c^{\text{HR}} \left(u + i - \frac{m}{2} + \Delta \mathbf{X}_{x,y}(i, j), v + j - \frac{n}{2} + \Delta \mathbf{Y}_{x,y}(i, j) \right) \quad (4)$$

the partial derivative of the element in the resampling kernel is simply the interpolated pixel value. Since the same kernel element is applied to three color channels, we need to sum up three color channels' value of the interpolated pixel to obtain the final partial derivative of the element in the resampling kernel.

The partial derivative of the kernel element offsets are computed as:

$$\begin{aligned} \frac{\partial \mathbf{p}_{x,y}^{\text{LR}}}{\partial \Delta \mathbf{X}_{x,y}(i, j)} &= \frac{\partial \mathbf{p}_{x,y}^{\text{LR}}}{\partial s_{u', v'}^{\text{HR}}} \cdot \frac{\partial s_{u', v'}^{\text{HR}}}{\partial \Delta \mathbf{X}_{x,y}(i, j)} \\ \frac{\partial \mathbf{p}_{x,y}^{\text{LR}}}{\partial \Delta \mathbf{Y}_{x,y}(i, j)} &= \frac{\partial \mathbf{p}_{x,y}^{\text{LR}}}{\partial s_{u', v'}^{\text{HR}}} \cdot \frac{\partial s_{u', v'}^{\text{HR}}}{\partial \Delta \mathbf{Y}_{x,y}(i, j)} \end{aligned} \quad (5)$$

because we employ bilinear interpolation to compute $s_{u', v'}^{\text{HR}}$, therefore, the partial derivative of the kernel offsets are defined as:

$$\begin{aligned} \frac{\partial \mathbf{p}_{x,y}^{\text{LR}}}{\partial \Delta \mathbf{X}_{x,y}(i, j)} &= \mathbf{K}_{x,y}(i, j) \cdot \sum_{c=RGB} (1 - \beta) \cdot (\mathbf{p}_{c, \lfloor u' \rfloor, \lfloor v' \rfloor + 1}^{\text{HR}} - \mathbf{p}_{c, \lfloor u' \rfloor, \lfloor v' \rfloor}^{\text{HR}}) + \\ &\quad \beta \cdot (\mathbf{p}_{c, \lfloor u' \rfloor + 1, \lfloor v' \rfloor + 1}^{\text{HR}} - \mathbf{p}_{c, \lfloor u' \rfloor + 1, \lfloor v' \rfloor}^{\text{HR}}) \\ \frac{\partial \mathbf{p}_{x,y}^{\text{LR}}}{\partial \Delta \mathbf{Y}_{x,y}(i, j)} &= \mathbf{K}_{x,y}(i, j) \cdot \sum_{c=RGB} (1 - \alpha) \cdot (\mathbf{p}_{c, \lfloor u' \rfloor + 1, \lfloor v' \rfloor}^{\text{HR}} - \mathbf{p}_{c, \lfloor u' \rfloor, \lfloor v' \rfloor}^{\text{HR}}) + \\ &\quad \alpha \cdot (\mathbf{p}_{c, \lfloor u' \rfloor + 1, \lfloor v' \rfloor + 1}^{\text{HR}} - \mathbf{p}_{c, \lfloor u' \rfloor, \lfloor v' \rfloor + 1}^{\text{HR}}) \end{aligned} \quad (6)$$

also because only one offset (in the horizontal and vertical direction) is associated with each element in the resampling kernel, we need to sum up partial derivative of each color component with respect to the offset to obtain the final partial derivative of the interpolated pixel value.

The pixel value of the downsampled image created using Equation 2 is inherently continuous floating point number. However, common image representation describes the color using integer number ranging from 0 to 255, thus, a quantization step is required. Since simply rounding the floating point number to its nearest integer number is not differentiable, during training we utilize the soft round method proposed by Nakanishi *et al.* [27] which is defined as:

$$\text{round}_{\text{soft}}(x) = x - \alpha \frac{\sin 2\pi x}{2\pi} \quad (7)$$

where α is a tuning parameter used to adjust the gradient around the integer position.

3.3 Image upscaling

The proposed CAR generation network is trained using back-propagation to maximize the SR performance, therefore, the

image upscaling module can be of any form of SR networks, even the differentiable bilinear or bicubic upscaling operations. After the seminal super-resolution model using deep learning proposed by Dong *et al.* [28], *i.e.*, the SRCNN, many state-of-the-art neural SR models have been proposed [29, 30, 31, 32, 33, 34, 35, 36, 37, 38, 39, 40]. More reviews and discussion about single image SR using deep learning can be referred to [8]. This paper employs state-of-the-art SR model EDSR [33] as the image upscaling module to guide the training of the proposed CAR generation network and to demonstrate the superiority of the learned image downscaling method for the SR task.

The EDSR is one of the state-of-the-art deep SR networks and its superior performance is benefited from the powerful residual learning techniques [26]. The EDSR is built on the success of the SRResNet [32] which achieved good performance by simply employing the ResNet [26] architecture on SR task. The EDSR enhanced SR performance by removing unnecessary part (Batch Normalization layer [41]) from the SRResNet and also applying a number of tweaks, such as adding residual scaling operation to stable the training process [33]. The SRNet part of Fig. 1 shows the architecture of the EDSR, it is composed of convolution layers converting the RGB image into feature spaces and a group of residual blocks refining feature maps. A global residual connection is employed to improve the efficiency of the gradient back-propagation. Finally, sub-pixel layers are utilized to upsample and transform features into target SR image.

3.4 Training objectives

One of the main contributions of our work is that we proposed a model to learn image downscaling without any supervision and signify that no constraint is applied to the downscaled image. The only objective guiding the generation of the downscaled image is the SR restoration error. The most common loss function generally defaults to the SR network training is the mean squared error (MSE) or the L2 norm loss, but it tends to lead to poor image quality as perceived by human observers [42]. Lim *et al.* [33] found that using another local metric, *e.g.*, L1 norm, can speed up the training process and produce better visual results. In order to improve the visual fidelity of the super-resolved image, perceptually-motivated metrics, such as SSIM [16] and MS-SSIM [43], and perceptual loss [44] are usually incorporated in the SR network training. To do fair comparisons with the EDSR, we only adopt the L1 norm loss as the restoration metric as suggested by [33]. The L1 norm loss defined for SR is as follows:

$$\mathcal{L}^{L_1}(\hat{\mathbf{I}}) = \frac{1}{N} \sum_{p \in \mathbf{I}} |\mathbf{p} - \hat{\mathbf{p}}| \quad (8)$$

where $\hat{\mathbf{I}}$ is the SR result, \mathbf{p} and $\hat{\mathbf{p}}$ represent the ground-truth and reconstructed pixel value, respectively.

Since we associate spatial offset for each element in the resampling kernel, and the offset is estimated without taking the neighborhoods of the kernel element into account. Independent kernel element offset may break the topology of the resampling kernel. To alleviate this problem, we suggest using the total offset distance of all kernel elements as the regularization loss which encourages kernel elements to stay in their rest position. Additionally, since the pixels indexed by the kernel elements that are far from the central position may have less correlation to the resampling result, we assign different weights to their

corresponding offset distance in terms of their position relative to the central position. The offset distance regularization term for a single resampling kernel is thus formulated as:

$$\mathcal{L}_{x,y}^{\text{offset}} = \sum_{i=0}^{m-1} \sum_{j=0}^{n-1} \gamma + \sqrt{\Delta \mathbf{X}_{x,y}(i, j)^2 + \Delta \mathbf{Y}_{x,y}(i, j)^2} \cdot w(i, j) \quad (9)$$

where $w(i, j) = \sqrt{(i - \frac{m}{2})^2 + (j - \frac{n}{2})^2} / \sqrt{\frac{m^2}{2} + \frac{n^2}{2}}$ is the normalized distance weight, the γ is introduced to act as the offset distance weight regulator.

The inconsistent resampling kernel offsets of spatially neighboring resampling kernels may cause pixel phase shift on the resulting LR images, which is manifested as objectionable jaggies, especially on the vertical and horizontal sharp edges (*e.g.*, the LR image in Fig. 5 (b)). To alleviate this phenomenon, we introduce the total variation (TV) loss [45] to constrain the movement of spatially neighboring resampling kernels. Instead of constraining the offsets on both vertical and horizontal directions, we only regularize vertical offsets on the horizontal direction and horizontal offsets on the vertical direction, which we name it the partial TV loss. Besides, variations of each resampling kernel offsets are weighted by its corresponding resampling kernel weights, leading to the following formula:

$$\begin{aligned} \mathcal{L}^{\text{TV}} = & \sum_{x,y} \left(\sum_{i,j} |\Delta \mathbf{X}_{x,y+1}(i, j) - \Delta \mathbf{X}_{x,y}(i, j)| \cdot \mathbf{K}(i, j) \right. \\ & \left. + \sum_{i,j} |\Delta \mathbf{Y}_{x+1,y}(i, j) - \Delta \mathbf{Y}_{x,y}(i, j)| \cdot \mathbf{K}(i, j) \right) \end{aligned} \quad (10)$$

Finally, the optimization objective of the entire framework is defined as:

$$\mathcal{L} = \mathcal{L}^{L_1} + \lambda \overline{\mathcal{L}^{\text{offset}}} + \gamma \mathcal{L}^{\text{TV}} \quad (11)$$

where the $\overline{\mathcal{L}^{\text{offset}}}$ is the mean offset distance regularization term of all resampling kernels, and λ is a scalar introduced to control the strength of offset distance regularization. γ is also a scalar used to tune the contribution of the partial TV loss to the final optimization objective.

4 EXPERIMENTS

4.1 Experimental setup

4.1.1 Datasets and metrics

For training the proposed content adaptive image downscaling resampler generation network under the guidance of EDSR, we employ the widely used DIV2K [46] image dataset. There are 1000 high-quality images in the DIV2K dataset, where 800 images for training, 100 images for validation and the other 100 images for testing. In the testing, four standard datasets, *i.e.*, the Set5 [47], Set14 [48], BSD100 [49] and Urban100 [50], are used as suggested by the EDSR paper [33]. Since we focus on how to downscale images without any supervision, therefore only HR images of the mentioned datasets are utilized. Following the setting in [33], we evaluate the peak noise-signal ratio (PSNR) and SSIM [16] on the Y channel of images represented in the YCbCr (Y, Cb, Cr) color space.

4.1.2 Implementation details

Regarding the implementation of the ResamplerNet, we first subtract the mean RGB value of the DIV2K training set. During the downsampling process, we gradually increase the channels of the output feature map from 3 to 128 using 3×3 convolution operation followed by the LeakyReLU activation. 5 residual blocks with each having features of 128 channels are used to model the context. For the two branches estimating the resampling kernels and offsets, we use the same architecture which is composed of ‘Conv-ReLU’ pairs with 256 feature channels, and a sub-pixel convolution is applied to upscale the input feature maps into resampling kernels and offsets with the same spatial size as the target downscaled image. For the configuration of the EDSR, we adopt the one with 32 residual blocks and 256 feature channels for each convolution in the residual block.

One of the important hyper-parameters must be determined is the resampling kernel size and the unit offset length. We define a 3×3 kernel size on the downscaled image space, and its actual size on the HR image space is $(3 \times s) \times (3 \times s)$, where s is the downscaling factor. The unit offset length is defined as one pixel on the downscaled image space whose corresponding unit length on the HR image space is s . For the offset distance weight regulator in Equation 9, we empirically set it to be 1.

The entire framework is trained on the DIV2K training set using the Adam optimizer [51] with $\beta_1 = 0.9$, $\beta_2 = 0.999$ and $\epsilon = 10^{-6}$. We set the mini-batch size as 16, and randomly crop the input HR image into 192×192 (for $4 \times$ downscale and SR) and 96×96 (for $2 \times$ downscale and SR) patches and augment it by applying random horizontal and vertical flips. During training, we conduct validation using 10 images from the DIV2K training set to select the trained model parameters, and the PSNR on validation is performed on full RGB channels [33]. The initial learning rate is 10^{-4} and halved every 150 epoch.

4.2 Evaluation of downscaling methods for SR

This section reports the quantitative and qualitative performance of different image downscaling methods for SR. Then ablation studies of the proposed CAR model is conducted. We compare the CAR model with four baseline methods, *i.e.*, the bicubic downscaling (Bicubic), and other three state-of-the-art image downscaling methods: perceptually optimized image downscaling (Perceptually) [15], detail-preserving image downscaling (DPID) [17], and L0-regularized image downscaling (L0-regularized) [19]. We train SR models using LR images downscaled by those four baseline downscaling algorithms and LR images downscaled by the proposed CAR model. The DPID requires to manually tune a hyper-parameter, which is content variant, to produce better perceptually favorable results. However, it is unpractical for us to generate large amount LR images by manually tuning, and also different people may have different perceptual preference. Thus, default value provided by the source code is adopted.

4.2.1 Quantitative and qualitative analysis

Table 1 summarizes the quantitative comparison results of different image downscaling methods for SR. It consists of two parts, one for bicubic upscaling and one for upscaling using the EDSR. We first analyze the SR performance using the EDSR, as

shown in Table 1 (Upscaling→EDSR), the proposed CAR model trained under the guidance of EDSR considerably boosts the PSNR metric against baselines over all the testing cases, and a noticeable gain on the SSIM metric is also obtained, which leads to a new state-of-the-art SR performance using the EDSR. The significant performance gain is benefited from the joint training of the CAR and EDSR in the end-to-end manner, where the goal of maximizing SR performance encourages the CAR to estimate better resamplers that produce the most suitable downscaled image for SR.

When compared to the SR performance of the LR images downscaled by bicubic interpolation, the three state-of-the-art image downscaling algorithms can hardly achieve more satisfying results, although the visual quality superiority of the downscaled images is reported by those original work. This is because those image downscaling methods are designed for better human perception thus the original information is changed considerably, which makes the downscaled image not well adapted to the SR defined by distortion metrics. Additionally, compared to the SR baseline of bicubic image downscaling, we note a significant performance drop on the perceptually based image downscaling baseline, this directly indicates that downscaled image produced by SSIM optimization cannot be well super-resolved by the state-of-the-art EDSR. The key reason can be illustrated as the SSIM optimization depends on patch selection which may lead to sub-pixel offset in the downscaled image. Other artifacts may underperform SR includes color splitting and noise exaggeration incurred during SSIM optimization [19].

In addition, we also evaluate SR performance of the CAR model trained under the guidance of bicubic interpolation based upscaling, and the bicubic downscaling is used as the baseline. As reported in Table 1 (Upscaling→Bicubic), the CAR model outperforms the fixed bicubic downscaling methods with a distinct margin in terms of upscaling using the fixed bicubic interpolation. The comparison results demonstrate the effectiveness of the proposed CAR model that it is flexible and can be trained under the guidance of differentiable upscaling operations, even if the upscaling operator is not learnable. With this discovery, the proposed CAR model can potentially replace the traditional and commonly used bicubic image downscaling operation under the hood, and end users can obtain extra image zoom in quality gain freely when using the bicubic interpolation for upscaling.

To further validate the effectiveness of the CAR image downscaling model, we evaluate the CAR model trained with another four state-of-the-art deep SR models, *i.e.*, SRDenseNet [34], D-DBPN [52], RDN [35] and RCAN [37], using $4 \times$ downscaling and upscaling factor on five testing datasets. We train all models using the DIV2K training dataset and all other training setup is set to be the same as described in Section 4.1.2. Table 2 presents the PSNR and SSIM of $4 \times$ upscaled images corresponding to LR images generated using the bicubic interpolation with anti-aliasing (MATLAB’s `imresize` function with default settings) and the CAR model. The experimental results (Bicubic and CAR \dagger) demonstrate a consistent performance gain of the SR task on images downscaled using the CAR model against that of the bicubic interpolation downscaling. When considering the SR performance of the CAR model trained under the guidance of the bicubic interpolation (Table 1) we can reasonably arrive at the conclusion that the CAR image downscaling model can

Table 1: Quantitative evaluation results (PSNR / SSIM) of different image downscaling methods for SR on benchmark datasets: Set5, Set14, BSD100, Urban100 and DIV2K (validation set).

Upscaling		Bicubic		EDSR				
Downscaling		Bicubic	CAR	Bicubic	Perceptually	DPID	L0-regularized	CAR
Set5	2x	33.66 / 0.9299	34.65 / 0.9440	37.62 / 0.9601	31.87 / 0.9252	36.79 / 0.9565	34.92 / 0.9496	38.12 / 0.9612
	4x	28.42 / 0.8104	29.00 / 0.8341	31.30 / 0.8818	25.18 / 0.7664	31.57 / 0.8889	30.88 / 0.8825	33.06 / 0.9101
Set14	2x	30.24 / 0.8688	31.11 / 0.8951	33.20 / 0.9145	29.31 / 0.8659	32.57 / 0.9094	31.30 / 0.8993	34.34 / 0.9282
	4x	26.00 / 0.7027	26.45 / 0.7324	28.06 / 0.7669	23.65 / 0.6526	28.15 / 0.7765	27.51 / 0.7676	29.57 / 0.8222
BSD100	2x	29.56 / 0.8431	30.27 / 0.8750	31.20 / 0.8983	28.93 / 0.8425	31.37 / 0.8913	30.55 / 0.8791	32.73 / 0.9081
	4x	25.96 / 0.6675	26.23 / 0.6970	27.20 / 0.7256	24.37 / 0.6278	27.20 / 0.7317	26.91 / 0.7268	28.55 / 0.7818
Urban100	2x	26.88 / 0.8403	27.60 / 0.8689	31.50 / 0.9234	26.52 / 0.8507	31.32 / 0.9223	29.74 / 0.9113	34.19 / 0.9482
	4x	23.14 / 0.6577	23.43 / 0.6875	25.12 / 0.7532	21.13 / 0.6093	25.76 / 0.7866	25.55 / 0.7865	27.71 / 0.8396
DIV2K (validation)	2x	31.01 / 0.9393	33.26 / 0.9330	36.23 / 0.9337	31.34 / 0.9008	35.17 / 0.9403	34.36 / 0.9327	37.46 / 0.9524
	4x	26.66 / 0.8521	28.47 / 0.8561	30.29 / 0.8240	25.61 / 0.7307	30.04 / 0.8336	29.68 / 0.8304	32.11 / 0.8691

Note: Red color indicates the best performance and Blue color represents the second.

Table 2: Evaluation results (PSNR / SSIM) of 4x upscaling using different SR networks on benchmark images downscaled by the CAR model.

Upscaling	Downscaling	Set5	Set14	BSD100	Urban100	DIV2K
SRDenseNet	Bicubic	31.40 / 0.8834	28.12 / 0.7701	27.23 / 0.7253	25.14 / 0.7532	30.34 / 0.8241
	CAR [†]	32.69 / 0.9057	29.44 / 0.8170	28.37 / 0.7739	27.53 / 0.8329	31.88 / 0.8629
	CAR [‡]	32.14 / 0.8985	29.02 / 0.8070	28.07 / 0.7639	26.76 / 0.8155	31.39 / 0.8504
D-DBPN	Bicubic	31.53 / 0.8861	28.21 / 0.7728	27.29 / 0.7276	25.31 / 0.7591	30.40 / 0.8263
	CAR [†]	32.61 / 0.9050	29.41 / 0.8174	28.38 / 0.7747	27.35 / 0.8292	31.84 / 0.8631
	CAR [‡]	32.19 / 0.8994	29.00 / 0.8059	28.07 / 0.7636	26.74 / 0.8145	31.44 / 0.8547
RDN	Bicubic	31.69 / 0.8881	28.31 / 0.7758	27.37 / 0.7312	25.46 / 0.7665	30.57 / 0.8301
	CAR [†]	32.81 / 0.9065	29.52 / 0.8191	28.43 / 0.7758	27.66 / 0.8368	31.98 / 0.8648
	CAR [‡]	32.61 / 0.9013	29.25 / 0.8129	28.32 / 0.7703	27.27 / 0.8309	31.50 / 0.8603
RCAN	Bicubic	31.56 / 0.8856	28.25 / 0.7739	27.33 / 0.7296	25.38 / 0.7633	30.52 / 0.8286
	CAR [†]	33.05 / 0.9092	29.69 / 0.8229	28.56 / 0.7797	27.99 / 0.8443	32.16 / 0.8680
	CAR [‡]	32.61 / 0.9043	29.35 / 0.8162	28.35 / 0.7750	27.82 / 0.8296	31.84 / 0.8638

CAR[†]: the CAR model is trained jointly with its corresponding SR model.

CAR[‡]: the SR model is trained using the downsampled images generated by the CAR model that is jointly with the EDSR.

Note: Red color indicates the best performance and Blue color represents the second.

be learned to adapt to SR models as long as the SR operation is differentiable.

In order to illustrate that the CAR image downscaling model can effectively preserve detailed information which can help SR models generally learn to better recover the original image content, we conduct another experiment in which the four state-of-the-art SR models are trained using LR images generated by the proposed CAR model trained jointly with the EDSR. Experimental results shown by the ‘CAR[‡]’ in Table 2 indicate that the performance of SR models trained using LR images generated by the CAR model trained jointly with the EDSR significantly surpasses that trained using images downsampled by the bicubic interpolation. We also observed that the performance gain of the CAR[‡] against the Bicubic is larger than the performance drop against the CAR[†]. The two findings lead to the conclusion that the CAR image downscaling model does preserve detailed information that are essential to superior SR using deep SR models.

A qualitative comparison of 4x downsampled image, produced by different downscaling methods, for SR is given in Fig. 3. As can be seen, the CAR model produces downsampled images that are super-resolved with the best visual quality when compared with that of the other four baselines trained using the EDSR. As

shown by the ‘Barbara’ example, due to strong aliasing occurred during downscaling by the four baseline methods, the EDSR cannot recover the correct direction of the parallel edge pattern formed by a stack of books. The downsampled image generated by the CAR incurs less aliasing and the EDSR well recovered the direction of the parallel edge pattern. For the ‘Comic’ example, we can observe that the CAR model preserves more details. Visual results of the ‘Monarch’ and ‘PPT3’ examples demonstrate that the SR of downsampled images produced by the CAR better restore continuous edges and produce sharper HR images.

4.2.2 Ablation studies

We conduct ablation experiments on the proposed CAR model to verify the effectiveness of our design. We mainly concern about the contribution of kernel element offset and the constraint on offset distance to the performance of the SR. Table 3 shows the quantitative ablation results, from which we can observe that the SR performance on all testing cases constantly increases with the addition of kernel element offset and the constraint on offset distance. The baseline model is the CAR without kernel element offset, meaning that the CAR only needs to estimate the resampling kernel weights which will be applied to the position defined by Equation 1 on the HR image (also



This figure is best viewed in color. Zoom in to see details of the downsampled image.

Figure 3: Qualitative results of 4x downsampled image and SR using the EDSR on four example images from the Set14 dataset.

Table 3: Ablation results (PSNR / SSIM) of the CAR model on the Set5, Set14, BSD100, Urban100 and DIV2K (validation set).

Model	Scale	Set5	Set14	BSD100	Urban100	DIV2K
CAR	2x	38.12 / 0.9612	34.34 / 0.9282	32.73 / 0.9081	34.19 / 0.9482	37.46 / 0.9524
CAR (w/o TV loss)	2x	38.47 / 0.9634	34.80 / 0.9345	33.14 / 0.9182	34.32 / 0.9505	37.87 / 0.9562
CAR (w/o offset constrain)	2x	38.10 / 0.9611	34.19 / 0.9257	32.98 / 0.9127	34.07 / 0.9484	37.12 / 0.9497
CAR (w/o offset)	2x	38.03 / 0.9597	34.13 / 0.9260	32.66 / 0.9108	33.66 / 0.9437	36.89 / 0.9429
CAR	4x	33.06 / 0.9101	29.57 / 0.8222	28.55 / 0.7818	27.71 / 0.8396	32.11 / 0.8691
CAR (w/o TV loss)	4x	33.61 / 0.9175	29.89 / 0.8326	29.04 / 0.8045	28.76 / 0.8672	32.72 / 0.8841
CAR (w/o offset constrain)	4x	32.79 / 0.9023	29.22 / 0.8082	28.24 / 0.7648	27.93 / 0.8406	31.91 / 0.8614
CAR (w/o offset)	4x	32.10 / 0.8951	28.79 / 0.7947	27.75 / 0.7526	27.53 / 0.8347	31.38 / 0.8520

Note: Red color indicates the best performance and Blue color represents the second.

illustrated as the pixel center in Fig. 2). Then, kernel element offset is incorporated, which brings a noticeable performance improvement in the 4x downscaling case than that of the 2x downscaling case. This is because on the 4x downscaling case, kernels are placed on the HR image with larger spacing, and much more information would get lost using regular resampling grid. Introducing kernel element offset makes the resampling kernel to be non-uniform and each element in the resampling kernel can seek to proper sampling position to better preserve useful information for the end SR task. Further SR performance is gained by add kernel element offset distance regularization. The kernel element offset distance regularization encourages the preservation of the resampling kernel topology and avoids unnecessary kernel element movement on the plain region with less structured texture, which potentially makes the training more stable and easier.

In order to better illustrate how the kernel offset distance regularization works, we visualized an example of resampling kernel element offsets (Fig. 4) with and without the offset distance regularization. We only visualize the central 9 of many kernel element offsets for a better demonstration. Fig. 4 (b) presents offsets by the CAR model trained without offset distance regularization. Fig. 4 (c) shows the resampling kernel element offsets estimated by the CAR model with resampling kernel offset regularization for the example image. It can be observed that kernel elements estimated by the CAR model trained with offset distance regularization only present obvious movement on the strong edge and textured region (the wheel ring and handle), and almost hold still at the rather smoothed region (the sky region). The kernel elements estimated by the CAR model trained without offset distance regularization also move towards the strong edges, however, it presents intensive movements on the plain region, which may lead to an unstable training process, thus, sub-optimal testing performance, since the gradient of the resampling kernel depends on the interpolated pixel value (Equation 4).

The superior SR performance achieved with the CAR model is benefited from the powerful capability of deep neural networks that can approximate arbitrary functions. However, without constraints on the enormous solution space, the deep model tends to find a tricky way to produce LR images preserving details that are in favor of generating accurate SR images but not for better human perception. Fig. 5 shows an example of 4x downsampled image by the CAR and 4x SR image by the jointly trained EDSR. As shown in Fig. 5 (b), the CAR model learned to preserve more information using much fewer

pixel spaces by arranging vertical edges in a regular criss-cross way, which makes the vertical edges in the LR image look jaggy. Jaggies are one type of aliasing that normally manifest as regular artifacts near sharp changes in intensity. But the human visual system finds regular artifacts more objectionable than irregular artifacts [53]. This problem is possibly caused by the inconsistent movement of the resampling kernels represented by the resampling kernel offsets near the sharp edges. To alleviate it, we introduced the partial TV loss of the horizontal and vertical resampling kernel offsets (Section 3.4) to constrain the rather free movements of the resampling kernel elements. As shown in Fig. 5 (c), we can observe a smoother LR image with much less unsightly artifacts.

By employing the partial TV loss of the resampling kernel offsets, the CAR model generates better images for perception. However, we also observed SR performance drop on each testing datasets, which is shown in the ‘CAR’ entries of Table 3. This is because the introduction of the partial TV loss breaks the optimal way of keeping information during downsampling. Other types of aliasing inevitably occurred on the sample-rate conversion, and the SR model cannot recover correct textures from those irregular patterns when compared with that of the regular jaggies. As illustrated by the SR patches shown in Fig. 5 (b) and (c), we can recognize that the SR image corresponding the jagged LR image can better represent the original HR patch than that corresponding to the perception friendly LR image. Additionally, we also observe a slightly more SR performance drop on the Urban100 dataset [50] in the 4x entry when the partial TV loss is employed, since images in the Urban100 are all buildings that are abundant of sharp edges and the CAR image downscaling model is more likely to produce criss-cross edge patterns that are easily super-resolved when the HR images are downsampled with large factor.

4.2.3 Comparison with public benchmark SR results

To compare the SR performance of the proposed CAR image downscaling model with other deep SR models trained neither on images downsampled using predefined operations (such as bicubic interpolation) or images downsampled by end-to-end trained task driven image downscaling models, we list several commonly compared public benchmark results on Table 4. The comparison is organized into two groups, *i.e.*, SR models trained with LR images produced using the bicubic interpolation method (‘Bicubic’ group) and LR images generated by models trained under the guidance of SR task (‘Learned’ group). In each group, it is further split into models trained using L2 loss function and

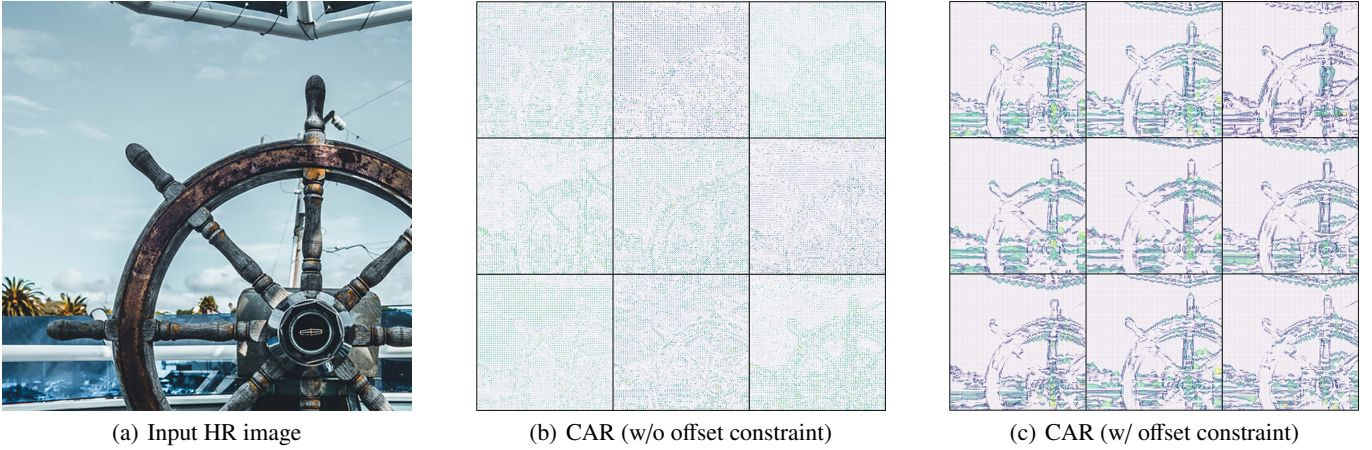


Figure 4: An example of 4 \times downscale resampling kernel element offsets.

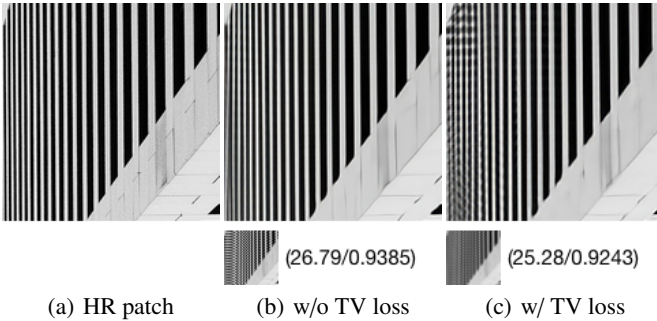


Figure 5: An example tradeoff between perception of the 4 \times downsampled image and distortion of the 4 \times SR image.

L1 loss function. SR models in the ‘Bicubic’ group include the SRCNN [28], VDSR [29], DRRN [54], MemNet [55], DnCNN [56], LapSRN [38], ZSSR [57], CARN [58], SRRAM [59]. In the ‘Learned’ group, we compare the CAR model with two recent state-of-the-art image downscaling models trained jointly with deep SR models, *i.e.*, the CNN-CR \rightarrow CNN-SR [4] model and the TAD \rightarrow TAU model [21].

As shown in Table 4, SR performance of upscaling models trained jointly with learnable image downscaling model outperform that of SR models trained using images downsampled in a predefined manner with a distinct margin. This is because that LR images generated by learnable image downscaling models adaptively preserve content dependent detailed information during downscaling, which essentially helps deep SR models learn to better recover original image content. In the ‘Learned’ group, SR models trained using L2 loss function achieve better performances on testing datasets than the same SR models trained using L1 loss function, since using L2 loss functions favors a high PSNR [33]. Comparing our model with recent state-of-the-art SR driven image downscaling models, the proposed model achieves the best performance on all testing datasets on the 4 \times image downscaling and upscaling track. On the 2 \times track, the proposed model achieves the best PSNR performance on four out of five testing datasets. It can be observed that the proposed model outperform the CNN-SR up to 1.17 dB on the Urban100

dataset [50]. This can be possibly explained by the reason that images of the Urban100 are all buildings with rich sharp edges, and CNN-CR (image downscaling model trained jointly with CNN-SR) are trained under the constraint of producing LR images similar to images downsampled by bicubic interpolation with pre-filtering, which inevitably constrain the edges of LR images generated by the CNN-CR to be blurry like that downsampled by the bicubic interpolation, and CNN-SR cannot well recover original edges from those blurred edges of the LR images. As to the proposed CAR model, it is trained without any LR constraint, since the resampling method naturally makes the LR result a valid image. Benefiting from the unsupervised training strategy, the CAR can adaptively preserve essential edge information for better super-resolution.

4.3 Evaluation of downsampled images

This section presents the analysis of the quality of the downsampled image produced by the CAR model from two perspectives. We first analyze the downsampled image in the frequency domain. We use the ‘Barbara’ image from the Set14 dataset as an example because it contains a wealth of high-frequency components (as shown in the first example of Fig. 3). Fig. 6 shows the spectrum obtained by applying FFT on the HR image and the downsampled images generated by the CAR model and four baseline downscaling methods. Each point in the spectrum represents a particular frequency contained in the spatial domain image. The point in the center of the spectrum is the DC component, and points closely around the center point represents low-frequency components. The further away from the center a point is, the higher is its corresponding frequency.

As shown by the spectrum of the HR image (Fig. 6 (a)), it contains a lot of high-frequency components. During image downscaling, spatial-aliasing is inevitably occurred since the sampling rate is below the Nyquist frequency. Aliasing can be spotted in the spectrum as spurious bands that are not presented in the spectrum of the HR image (high frequency component is aliased into low frequency), *e.g.*, the blue box marked region of Fig. 6 (b-f). One way to remove aliasing is to use a blurry filter upon resampling (so does the default MATLAB `imresize` function). As shown by the red box marked region of Fig. 6

Table 4: Public benchmark results (PSNR / SSIM) of $2\times$ and $4\times$ upscaling using different SR networks on the Set5, Set14, BSD100, Urban100 and DIV2K validation set.

Downscaling type	Loss	Upscaling	Set5	Set14	BSD100	Urban100	DIV2K
Bicubic	L2	SRCCN	36.66 / 0.9542	32.42 / 0.9063	31.36 / 0.8897	29.50 / 0.8946	33.05 / 0.9581
		VDSR	37.53 / 0.9587	33.03 / 0.9213	31.90 / 0.8960	30.76 / 0.9140	33.66 / 0.9625
		DRRN	37.74 / 0.9591	33.23 / 0.9136	32.05 / 0.8973	31.23 / 0.9188	35.63 / 0.9410
		MemNet	37.78 / 0.9597	33.28 / 0.9142	32.08 / 0.8978	31.31 / 0.9195	- / -
		DnCNN	37.58 / 0.9590	33.03 / 0.9118	31.90 / 0.8961	30.74 / 0.9139	- / -
	L1	LapSRN	37.52 / 0.9590	33.08 / 0.9130	31.80 / 0.8950	30.41 / 0.9100	35.31 / 0.9400
		ZSSR	37.37 / 0.9570	33.00 / 0.9108	31.65 / 0.8920	- / -	- / -
		CARN	37.76 / 0.9590	33.52 / 0.9166	32.09 / 0.8978	31.92 / 0.9256	36.04 / 0.9451
		SRRAM	37.82 / 0.9592	33.48 / 0.9171	32.12 / 0.8983	32.05 / 0.9264	- / -
		ESRGAN	- / -	- / -	- / -	- / -	- / -
Learned	L2	CNN-SR	38.88 / -	35.40 / -	33.92 / -	33.68 / -	- / -
		Our's	38.95 / 0.9648	35.82 / 0.9393	33.87 / 0.9220	35.36 / 0.9555	38.41 / 0.9582
	L1	TAU	37.69 / -	33.90 / -	32.62 / -	31.96 / -	36.13 / -
		Our's	38.12 / 0.9612	34.34 / 0.9282	32.73 / 0.9081	34.19 / 0.9482	37.46 / 0.9524
Bicubic	L2	SRCCN	30.48 / 0.8628	27.49 / 0.7503	26.90 / 0.7101	24.52 / 0.7221	27.78 / 0.8753
		VDSR	31.35 / 0.8838	28.01 / 0.7674	27.29 / 0.7251	25.18 / 0.7524	28.17 / 0.8841
		SRResNet	32.05 / 0.8910	28.53 / 0.7804	27.57 / 0.7354	26.07 / 0.7839	- / -
		DRRN	31.68 / 0.8888	28.21 / 0.7720	27.38 / 0.7284	25.44 / 0.7638	29.98 / 0.8270
		MemNet	31.74 / 0.8893	28.26 / 0.7723	27.40 / 0.7281	25.50 / 0.7630	- / -
		DnCNN	31.40 / 0.8845	28.04 / 0.7672	27.29 / 0.7253	25.20 / 0.7521	- / -
	L1	LapSRN	31.54 / 0.8850	28.19 / 0.7720	27.32 / 0.7280	25.21 / 0.7560	29.88 / 0.8250
		ZSSR	31.13 / 0.8796	28.01 / 0.7651	27.12 / 0.7211	- / -	- / -
		CARN	32.13 / 0.8937	28.60 / 0.7806	27.58 / 0.7349	26.07 / 0.7837	30.43 / 0.8374
		SRRAM	32.13 / 0.8932	28.54 / 0.7800	27.56 / 0.7350	26.05 / 0.7834	- / -
		ESRGAN	32.73 / 0.9011	28.99 / 0.7917	27.85 / 0.7455	27.03 / 0.8153	- / -
Learned	L2	CNN-SR	- / -	- / -	- / -	- / -	- / -
		Our's	34.15 / 0.9203	30.60 / 0.8424	29.48 / 0.8090	29.31 / 0.8704	33.16 / 0.8866
	L1	TAU	31.59 / -	28.36 / -	27.57 / -	25.56 / -	30.25 / -
		Our's	33.06 / 0.9101	29.57 / 0.8222	28.55 / 0.7818	27.71 / 0.8396	32.11 / 0.8691

Note: Red color indicates the best performance and Blue color represents the second.

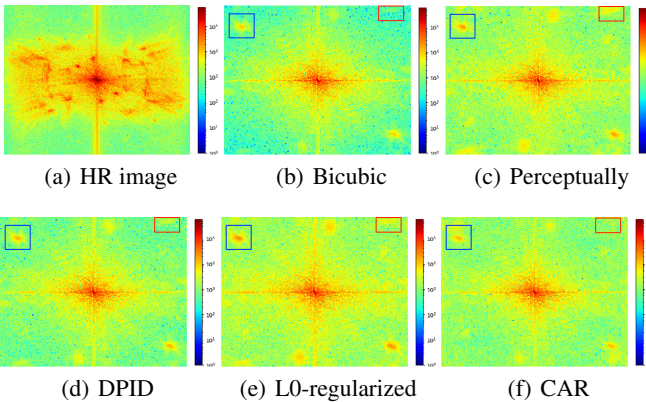


Figure 6: Spectrum analysis of the $4\times$ downsampled ‘Barbara’ image in the Set14 dataset using different downscaling methods.

(b), aliasing of the downsampled image produced by the MATLAB `imresize` function is alleviated. Of course, the problem with this approach is that it makes the image blurry, *i.e.*, lost of high-frequency components, which is also illustrated by Fig. 6 (b) that the magnitude of high-frequency components far from the center is lower than that of the spectrum of the HR image. When comparing the spectrum of the CAR and other three baseline methods produced image with that of the bicubic one, we

Table 5: Bpp of lossless compressed downsampled images using the JPEG-LS

		Bicubic	Perceptually	DPID	L0	CAR
Set5	2x	11.99	13.27	12.65	16.10	11.5
		11.23	12.01	12.05	15.07	10.82
		11.11	11.9	11.8	15.31	10.47
		11.39	12.22	12.19	15.27	11.04
		10.42	11.38	11.1	14.04	10.01
		11.228	12.156	11.958	15.158	10.768
Set5	4x	14.78	16.52	15.32	17.41	14.51
		12.61	14.27	13.32	15.19	12.55
		12.85	14.42	13.51	15.59	12.67
		12.23	14.26	12.94	14.97	12.47
		11.54	13.46	12.14	13.91	11.51
		12.802	14.586	13.446	15.414	12.742

Note: Red color indicates the best performance and Blue color represents the second.

can observe much more high-frequency components have been preserved. On the other side, compared with the spectrum of image produced by the three state-of-the-art image downscaling baselines (Fig. 6 (c-e)), the spectrum of the CAR generated image demonstrates less aliasing at some frequency band.

Additionally, we analyze the downsampled image from the perspective of lossless compression performance. Table 5 reports the average bits-per-pixel (bpp) of the lossless compressed images using the lossless JPEG (JPEG-LS) [60]. It is obvious that the downsampled image produced by the CAR model can be more

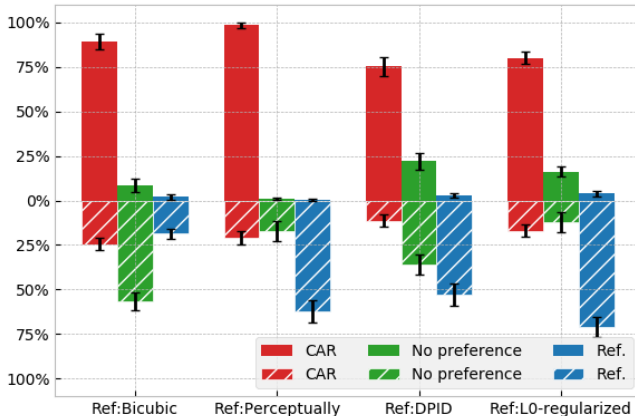


Figure 7: User study results comparing the proposed CAR model against reference image downscaling algorithms for the image super-resolution and image downscaling tasks. Each data point is an average over valid records evaluated on 20 image groups and the error bars indicate 95% confidence interval. The upper part (above the zero axes) is the image quality preference of the SR task, and the lower part (below the zero axes) is the image quality preference of the image downscaling task.

easily compressed than that by downscaling algorithms designed for better human perception because the compressed results of the CAR downscaled images have fewer bpp. When compared with the bpp of compressed bicubic downscaled images, the CAR model achieves similar but slightly better compression performance.

4.4 User study

To evaluate the visual quality of the generated SR images and LR images corresponding to different downscaling algorithms, we conduct user study which is widely adopted in many image generation tasks. We pick 20 sample images from different testing datasets, *i.e.*, the Set5, Set14, BSD100, and Urban100 dataset. From each one, 5 images are randomly selected with diverse properties, including people, animal, building, natural scenes and computer-generated graphics. We adopt similar evaluation settings used in [14, 15, 17, 19]. The user study are conducted as the A/B testing: the original image is presented in the middle place with two variants (SR images or downscaled images) showed in either side, among which one is produced by the CAR method and another is generated by one of the competing methods, *i.e.*, Bicubic, Perceptually [15], DPID [17] and L0-regularized [19]. The users are required to ask the question ‘which one looks better’ by exclusively selecting one of the three options from: 1) A is better than B; 2) A equals to B; 3) B is better than A. For all 20 sample images, there are 80 pairwise decisions for each user, and all image pairs are shown in random temporal order and the two variants of the original image of a pair are also randomly shown in position A or position B. To test the reliability of the user study result, we add additional 10 image groups by randomly repeating question from the 80 image groups. All images are showed at native resolution of the display and zoom functionality of the UI is disabled. Users can

only pan the view if the total size of a group of images exceeds the screen resolution. We do not impose any other restrictions on the viewing way, users can judge those images at any viewing distance and angle without time limits.

We invited 34 participants for both the user study on 4x image super-resolution and 4x image downscaling tasks. Answers from each participant are filtered out if it achieves less than 80% consistency [14, 15] on the repeated 10 questions, which generates 33 and 30 valid records for the image super-resolution and image downscaling tasks, respectively. As can be seen from Fig. 7, the total preferences of the SR and image downscaling task opted for the CAR model are larger than that of the reference methods. The upper part (above the zero axes) of Fig. 7 shows the results of the user study on 4x image super-resolution task, each group of bars present the comparison between SR images corresponding to the CAR generated LR images and SR images corresponding to LR images produced by the reference method. The results indicate that the CAR model achieves at least 75% preference over all other algorithms. Besides, our algorithm achieves more than 98% preference compared with the Perceptually based [15] downsampled image and the original HR image. Although there are about 25% and 20% preference on ‘A equals to B’ plus ‘B is better than A’ on the DPID and L0-regularized entry, respectively, it still cannot compete with the significant superiority of the CAR method. When combined with the objective metrics presented in Table 1, we can arrive at the conclusion that LR images produced by algorithms solely optimized for better human perception cannot be well recovered.

The lower part (below the zero axes) of Fig. 7 shows the users’ perceptual preference for the 4x downscaled images generated by the CAR method versus the Bicubic, Perceptually, DPID, and L0-regularized image downscaling algorithms. We observed that the CAR method gets less preference when compared with that of the Perceptually, DPID, and L0-regularized algorithm, which illustrates that the three state-of-the-art algorithms generate more perceptually favored LR images. However, when compared with the Bicubic downscaling algorithm, the user preference for the CAR method is slightly higher than that for the Bicubic, and at most cases, participants tend to give no preference for both methods. This indicates that the CAR image downscaling method is comparable to the bicubic downscaling algorithm in terms of human perception. Among the three state-of-the-art image downscaling algorithms, the DPID achieves less agreement since its hyper-parameter is content dependent, but during the test, the default value is used. The perceptually based image downscaling and the L0-regularized method achieve more than 60% user preference because these methods artificially emphasize the edges of image content, which can be good if the image is going to be displayed at a very small size, such as an icon. Whether it is desirable in other cases is debatable. It does tend to make images look better at first glance, but at the expense of realism in terms of signal fidelity.

5 CONCLUSION

This paper introduces the CAR model for image downscaling, which is an end-to-end system trained by maximizing the SR performance. It simultaneously learns a mapping for resolution

reduction and SR performance improvement. One major contribution of our work is that the CAR model is trained in an unsupervised manner meaning that there is no assumption on how the original HR image will be downsampled, which helps the image downscale model to learn to keep essential information for SR task in a more optimal way. This is achieved by the content adaptive resampling kernel generation network which estimates spatial non-uniform resampling kernels for each pixel in the downsampled image according to the input HR image. The downsampled pixel value is obtained by decimating HR pixels covered by the resampling kernel. Our experimental results illustrate that the CAR model trained jointly with the SR networks achieves a new state-of-the-art SR performance while produces downsampled images whose quality are comparable to that of the widely adopted image downscaling method.

REFERENCES

- [1] A. M. Bruckstein, M. Elad, and R. Kimmel. Down-scaling for better transform compression. *IEEE Trans. Image Process.*, 12(9):1132–1144, Sep. 2003. ISSN 1057-7149. doi: 10.1109/TIP.2003.816023.
- [2] W. Lin and Li Dong. Adaptive downsampling to improve image compression at low bit rates. *IEEE Trans. Image Process.*, 15(9):2513–2521, Sep. 2006. ISSN 1057-7149. doi: 10.1109/TIP.2006.877415.
- [3] Y. Zhang, D. Zhao, J. Zhang, R. Xiong, and W. Gao. Interpolation-dependent image downsampling. *IEEE Trans. Image Process.*, 20(11):3291–3296, Nov. 2011. ISSN 1057-7149. doi: 10.1109/TIP.2011.2158226.
- [4] Y. Li, D. Liu, H. Li, L. Li, Z. Li, and F. Wu. Learning a convolutional neural network for image compact-resolution. *IEEE Trans. Image Process.*, 28(3):1092–1107, March 2019. ISSN 1057-7149. doi: 10.1109/TIP.2018.2872876.
- [5] Claude E. Shannon. Communication in the presence of noise. *Proc. IEEE*, 86(2):447–457, Feb. 1998.
- [6] J. Yang, J. Wright, T. S. Huang, and Y. Ma. Image super-resolution via sparse representation. *IEEE Trans. Image Process.*, 19(11):2861–2873, Nov. 2010. ISSN 1057-7149. doi: 10.1109/TIP.2010.2050625.
- [7] Jianchao Yang and Thomas S Huang. *Image super-resolution: Historical overview and future challenges*, pages 1–33. CRC, 1 2017.
- [8] W. Yang, X. Zhang, Y. Tian, W. Wang, J. Xue, and Q. Liao. Deep learning for single image super-resolution: A brief review. *IEEE Trans. Multimedia*, pages 1–1, 2019.
- [9] Saeed Anwar, Salman Khan, and Nick Barnes. A deep journey into super-resolution: A survey, 2019. URL <https://arxiv.org/abs/1904.07523>.
- [10] George Wolberg. *Digital image warping*, volume 10662. IEEE CS, 1990.
- [11] L. Fang, O. C. Au, K. Tang, and A. K. Katsaggelos. Antialiasing filter design for subpixel downsampling via frequency-domain analysis. *IEEE Trans. Image Process.*, 21(3):1391–1405, March 2012. ISSN 1057-7149. doi: 10.1109/TIP.2011.2165550.
- [12] Don P. Mitchell and Arun N. Netravali. Reconstruction filters in computer-graphics. *SIGGRAPH Comput. Graph.*, 22(4):221–228, june 1988. ISSN 0097-8930.
- [13] Claude E. Duchon. Lanczos filtering in one and two dimensions. *J. Appl. Meteor.*, 18(8):1016–1022, Aug. 1979.
- [14] Johannes Kopf, Ariel Shamir, and Pieter Peers. Content-adaptive image downscaling. *ACM Trans. Graph.*, 32(6):173:1–173:8, Nov. 2013.
- [15] A. Cengiz Öztireli and Markus Gross. Perceptually based downscaling of images. *ACM Trans. Graph.*, 34(4):77:1–77:10, July 2015.
- [16] Zhou Wang, Alan Conrad Bovik, Hamid Rahim Sheikh, and Eero P. Simoncelli. Image quality assessment: from error visibility to structural similarity. *IEEE Trans. Image Process.*, 13(4):600–612, April 2004.
- [17] Nicolas Weber, Michael Waechter, Sandra C. Amend, Stefan Guthe, and Michael Goesele. Rapid, detail-preserving image downscaling. *ACM Trans. Graph.*, 35(6):205:1–205:6, Nov. 2016.
- [18] Eduardo S. L. Gastal and Manuel M. Oliveira. Spectral remapping for image downscaling. *ACM Trans. Graph.*, 36(4):145:1–145:16, July 2017.
- [19] Junjie Liu, Shengfeng He, and Rynson W. H. Lau. l_0 -regularized image downscaling. *IEEE Trans. Image Process.*, 27(3):1076–1085, March 2018.
- [20] Xianxu Hou, Yuanhao Gong, Bozhi Liu, Ke Sun, Jingxin Liu, Bolei Xu, Jiang Duan, and Guoping Qiu. Learning based image transformation using convolutional neural networks. *IEEE Access*, 6:49779–49792, Sep. 2018.
- [21] Heewon Kim, Myungsub Choi, Bee Lim, and Kyoung Mu Lee. Task-aware image downscaling. In *Proceedings of the European Conference on Computer Vision*, pages 399–414, 2018.
- [22] Bert De Brabandere, Xu Jia, Tinne Tuytelaars, and Luc Van Gool. Dynamic filter networks. In *Proceedings of the 30th International Conference on Neural Information Processing Systems*, pages 667–675, 2016.
- [23] Jürgen Schmidhuber. *Evolutionary principles in self-referential learning, or on learning how to learn: the meta-meta-... hook*. PhD thesis, Technische Universität München, 1987.
- [24] Jifeng Dai, Haozhi Qi, Yuwen Xiong, Yi Li, Guodong Zhang, Han Hu, and Yichen Wei. Deformable convolutional networks. In *IEEE International Conference on Computer Vision*, pages 764–773, 2017.
- [25] Fisher Yu and Vladlen Koltun. Multi-scale context aggregation by dilated convolutions. In *International Conference on Learning Representations*, 2016.
- [26] Kaiming He, Xiangyu Zhang, Shaoqing Ren, and Jian Sun. Deep residual learning for image recognition. In *IEEE Conference on Computer Vision and Pattern Recognition*, pages 770–778, 2016.
- [27] Ken M. Nakanishi, Shin-ichi Maeda, Takeru Miyato, and Daisuke Okanohara. Neural multi-scale image compression. In *Computer Vision*, pages 718–732, 2019.

[28] Chao Dong, Chen Change Loy, Kaiming He, and Xiaoou Tang. Image super-resolution using deep convolutional networks. *IEEE Trans. Pattern Anal. Mach. Intell.*, 38(2):295–307, Feb. 2016.

[29] Jiwon Kim, Jung Kwon Lee, and Kyoung Mu Lee. Accurate image super-resolution using very deep convolutional networks. In *IEEE Conference on Computer Vision and Pattern Recognition*, pages 1646–1654, 2016.

[30] Jiwon Kim, Jung Kwon Lee, and Kyoung Mu Lee. Deeply-recursive convolutional network for image super-resolution. In *IEEE Conference on Computer Vision and Pattern Recognition*, pages 1637–1645, 2016.

[31] Wenzhe Shi, Jose Caballero, Ferenc Huszár, Johannes Totz, Andrew P. Aitken, Rob Bishop, Daniel Rueckert, and Zehan Wang. Real-time single image and video super-resolution using an efficient sub-pixel convolutional neural network. In *IEEE Conference on Computer Vision and Pattern Recognition*, pages 1874–1883, 2016.

[32] Christian Ledig, Lucas Theis, Ferenc Huszár, Jose Caballero, Andrew Cunningham, Alejandro Acosta, Andrew Aitken, Alykhan Tejani, Johannes Totz, Zehan Wang, and Wenzhe Shi. Photo-realistic single image super-resolution using a generative adversarial network. In *IEEE Conference on Computer Vision and Pattern Recognition*, pages 105–114, 2017.

[33] Bee Lim, Sanghyun Son, Heewon Kim, Seungjun Nah, and Kyoung Mu Lee. Enhanced deep residual networks for single image super-resolution. In *IEEE Conference on Computer Vision and Pattern Recognition Workshops*, pages 1132–1140, 2017.

[34] T. Tong, G. Li, X. Liu, and Q. Gao. Image super-resolution using dense skip connections. In *IEEE International Conference on Computer Vision*, pages 4809–4817, 2017.

[35] Yulun Zhang, Yapeng Tian, Yu Kong, Bineng Zhong, and Yun Fu. Residual dense network for image super-resolution. In *IEEE Conference on Computer Vision and Pattern Recognition*, pages 2472–2481, 2018.

[36] Kai Zhang, Wangmeng Zuo, and Lei Zhang. Learning a single convolutional super-resolution network for multiple degradations. In *IEEE Conference on Computer Vision and Pattern Recognition*, pages 3262–3271, 2018.

[37] Yulun Zhang, Kunpeng Li, Kai Li, Lichen Wang, Bineng Zhong, and Yun Fu. Image super-resolution using very deep residual channel attention networks. In *Proceedings of the European Conference on Computer Vision*, pages 286–301, 2018.

[38] W. Lai, J. Huang, N. Ahuja, and M. Yang. Fast and accurate image super-resolution with deep laplacian pyramid networks. *IEEE Trans. Pattern Anal. Mach. Intell.*, pages 1–1, Aug. 2018. ISSN 0162-8828. doi: 10.1109/TPAMI.2018.2865304.

[39] Kai Zhang, Wangmeng Zuo, and Lei Zhang. Deep plug-and-play super-resolution for arbitrary blur kernels. In *IEEE Conference on Computer Vision and Pattern Recognition*, pages 1671–1681, 2019.

[40] Tao Dai, Jianrui Cai, Yongbing Zhang, Shu-Tao Xia, and Lei Zhang. Second-order attention network for single image super-resolution. In *IEEE Conference on Computer Vision and Pattern Recognition*, pages 11065–11074, 2019.

[41] Sergey Ioffe and Christian Szegedy. Batch normalization: Accelerating deep network training by reducing internal covariate shift. In *Proceedings of the 32nd International Conference on International Conference on Machine Learning*, pages 448–456, 2015.

[42] Hang Zhao, Orazio Gallo, Iuri Frosio, and Jan Kautz. Loss functions for image restoration with neural networks. *IEEE Trans. Comput. Imag.*, 3(1):47–57, March 2017.

[43] Zhou Wang, Eero P. Simoncelli, and Alan Conrad Bovik. Multiscale structural similarity for image quality assessment. In *The Thirty-Seventh Asilomar Conference on Signals, Systems Computers*, pages 1398–1402, 2003.

[44] Justin Johnson, Alexandre Alahi, and Li Fei-Fei. Perceptual losses for real-time style transfer and super-resolution. In *Proceedings of the European conference on computer vision*, pages 694–711, 2016.

[45] Leonid I Rudin, Stanley Osher, and Emad Fatemi. Nonlinear total variation based noise removal algorithms. *PHYS-ICA D.*, 60(1-4):259–268, Nov. 1992.

[46] Eirikur Agustsson and Radu Timofte. Ntire 2017 challenge on single image super-resolution: Dataset and study. In *IEEE Conference on Computer Vision and Pattern Recognition Workshops*, pages 1122–1131, 2017.

[47] Marco Bevilacqua, Aline Roumy, Christine Guillemot, and Marie-Line Alberi Morel. Low-complexity single-image super-resolution based on nonnegative neighbor embedding. In *British Machine Vision Conference*, 2012.

[48] Roman Zeyde, Michael Elad, and Matan Protter. On single image scale-up using sparse-representations. In *Proceedings of the 7th International Conference on Curves and Surfaces*, pages 711–730, 2012.

[49] David R. Martin, Charless Fowlkes, D. Tal, and Jitendra Malik. A database of human segmented natural images and its application to evaluating segmentation algorithms and measuring ecological statistics. In *IEEE International Conference on Computer Vision*, pages 416–423, 2001.

[50] JiaBin Huang, Abhishek Singh, and Narendra Ahuja. Single image super-resolution from transformed self-exemplars. In *IEEE Conference on Computer Vision and Pattern Recognition*, pages 5197–5206, 2015.

[51] Diederik P. Kingma and Jimmy Ba. Adam: A method for stochastic optimization. In *International Conference on Learning Representations*, 2015.

[52] Muhammad Haris, Greg Shakhnarovich, and Norimichi Ukita. Deep back-projection networks for super-resolution. In *IEEE Conference on Computer Vision and Pattern Recognition*, pages 1664–1673, 2018.

[53] Robert L. Cook. Stochastic sampling in computer graphics. *ACM Trans. Graph.*, 5(1):51–72, Jan. 1986. ISSN 0730-0301.

[54] Y. Tai, J. Yang, and X. Liu. Image super-resolution via deep recursive residual network. In *IEEE Conference on Computer Vision and Pattern Recognition*, pages 2790–2798, 2017.

- [55] R. Chen, Y. Qu, K. Zeng, J. Guo, C. Li, and Y. Xie. Persistent memory residual network for single image super resolution. In *IEEE Conference on Computer Vision and Pattern Recognition Workshops*, 2018.
- [56] K. Zhang, W. Zuo, Y. Chen, D. Meng, and L. Zhang. Beyond a gaussian denoiser: Residual learning of deep cnn for image denoising. *IEEE Trans. Image Process.*, 26(7):3142–3155, July 2017. ISSN 1057-7149. doi: 10.1109/TIP.2017.2662206.
- [57] A. Shocher, N. Cohen, and M. Irani. Zero-shot super-resolution using deep internal learning. In *IEEE Conference on Computer Vision and Pattern Recognition*, pages 3118–3126, 2018.
- [58] Namhyuk Ahn, Byungkon Kang, and Kyung-Ah Sohn. Fast, accurate, and lightweight super-resolution with cascading residual network. In *Proceedings of the European Conference on Computer Vision*, pages 252–268, 2018.
- [59] Jun-Hyuk Kim, Jun-Ho Choi, Manri Cheon, and Jong-Seok Lee. Ram: Residual attention module for single image super-resolution, 2018. URL <https://arxiv.org/abs/1811.12043>.
- [60] M. J. Weinberger, G. Seroussi, and G. Sapiro. The loco-i lossless image compression algorithm: principles and standardization into jpeg-ls. *IEEE Trans. Image Process.*, 9(8):1309–1324, Aug. 2000.